frontiers | Frontiers in Astronomy and Space Sciences

TYPE Brief Research Report
PUBLISHED 31 May 2024
DOI 10.3389/fspas.2024.1394817

OPEN ACCESS

EDITED BY
Gian Luca Delzanno,
Los Alamos National Laboratory (DOE), United States

REVIEWED BY
Kareem Sorathia,
Johns Hopkins University, United States
Justin Holmes,
Los Alamos National Laboratory (DOE), United States

*CORRESPONDENCE
K. Seki,
k.seki@eps.s.u-tokyo.ac.jp

RECEIVED 02 March 2024
ACCEPTED 29 April 2024
PUBLISHED 31 May 2024

CITATION
Seki K, Matsumoto Y, Terada N, Hara T, Brain DA, Nakagawa H, McFadden JP, Halekas JS, Ruhunusiri S, Mitchell DL, Andersson L, Espley JR, Baker DN, Luhmann JG and Jakosky BM (2024), Characteristics of plasma boundaries with large density gradients and their effects on Kelvin–Helmholtz instability.
Front. Astron. Space Sci. 11:1394817.
doi: 10.3389/fspas.2024.1394817

Characteristics of plasma boundaries with large density gradients and their effects on Kelvin–Helmholtz instability

K. Seki[1]*, Y. Matsumoto[2], N. Terada[3], T. Hara[4], D. A. Brain[5], H. Nakagawa[3], J. P. McFadden[4], J. S. Halekas[6], S. Ruhunusiri[5], D. L. Mitchell[4], L. Andersson[5], J. R. Espley[7], D. N. Baker[5], J. G. Luhmann[4] and B. M. Jakosky[5]

[1]Department of Earth and Planetary Science, Graduate School of Science, University of Tokyo, Tokyo, Japan, [2]Institute for Advanced Academic Research, Chiba University, Chiba, Japan, [3]Graduate School of Science, Tohoku University, Sendai, Japan, [4]Space Sciences Laboratory, University of California, Berkeley, CA, United States, [5]Laboratory for Atmospheric and Space Physics, University of Colorado, Boulder, CO, United States, [6]Department of Physics and Astronomy, University of Iowa, Iowa City, IA, United States, [7]NASA Goddard Space Flight Center, Greenbelt, MD, United States

Boundaries between space plasmas occur in numerous contexts and scales, from astrophysical jets to planetary magnetospheres. Mass and momentum transport across boundaries poses a fundamental problem in magnetospheric physics. Kelvin–Helmholtz instability (KHI) is a promising mechanism to facilitate transport. Although previous studies have suggested KHI occurrence in various space plasmas, theory predicts that compressibility prevents KHI excitation at boundaries with large density gradients because of previously considered boundary structures where density varies with velocity. Based on the observations of a large density gradient boundary by MAVEN at Mars, where we can observe an extreme case, in this study, we show that it is the entropy, instead of the previously considered density, that varies with the velocity in the real velocity-sheared boundary. The entropy-based boundary structure places the velocity shear in a lower-density region than the traditional density-based structure and weakens the compressibility effect. This new boundary structure thus enables KHI excitation even at large density gradient boundaries, such as at the ionopause of unmagnetized planets and the plasmapause of magnetized planets. The result suggests the ubiquitous occurrence of KHI in the plasma universe and emphasizes its important role in planetary cold plasma escape from unmagnetized planets.

KEYWORDS

Kelvin–Helmholtz instability, Mars, density gradient, compressibility, cold plasma, MAVEN

1 Introduction

Momentum and mass transport mechanisms at a velocity-sheared boundary in the space plasma are important processes that affect the supply of magnetospheric plasma at various planets. In various space plasmas, collisions are often negligible (Matthaeus et al., 2003), and thus, momentum and mass transport primarily occurs through couplings between constituent charged particles and the electric/magnetic fields (Seki et al., 2003). When two

different plasma regimes come into contact, instabilities facilitate mass and momentum transport across the ambient magnetic field. Such boundaries occur in numerous contexts and scales from astrophysical plasmas such as at neutron star mergers (Price and Rosswog, 2006), star-forming molecular clouds (Berne et al., 2010), nova explosions (Casanova et al., 2011), and solar corona (Hillier and Arregui, 2019), in addition to various planetary magnetospheres (Hasegawa et al., 2004; Slavin et al., 2008; Delamere et al., 2013). The Kelvin–Helmholtz instability (KHI) (Fujimoto and Terasawa, 1994) is considered a promising candidate to facilitate momentum and mass transfers across boundaries.

One of the important parameters for assessment of the occurrence of KHI is compressibility. The stability analysis of compressional plasma predicts that KHI excitation is suppressed when the density ratio across the boundary (r_n) becomes larger, due to the stabilizing effects of the compressibility with a high Mach number ($M_f > 2$, where M_f represents the magnetosonic Mach number) (Miura and Pritchett, 1982). An experimental study indicates a reduction in the growth rate of KHI and supports the theoretical prediction (Wan et al., 2015). In theoretical considerations, both the velocity shear and density gradient are often expressed with the hyperbolic tangent (Miura and Pritchett, 1982; Amerstorfer et al., 2010; Matsumoto and Seki, 2010). This traditional density-based model of the velocity-sheared boundary has a high M_f region in the middle of the boundary, and the KHI suppression by compressibility can become significant in large density gradient cases.

In Earth, which has a strong intrinsic magnetic field, KHI has been identified by *in situ* satellite observations at the boundary between the shocked solar wind and terrestrial magnetosphere (Hasegawa et al., 2004), where the density gradient is usually small (with the density ratio between the two sides of the boundary being $r_n < 100$) and compressibility is not very important. The in-plane magnetic field (magnetic field parallel to velocity) also stabilizes KHI in the low r_n regime, and the magnetic field geometry effects are pronounced enough to excite KHI in the Earth's magnetosphere (Kavosi et al., 2023). Thus, the KHI excitation at the magnetopause depends on the dipole tilt angle and interplanetary magnetic field (IMF) (Hwang et al., 2023). KHI can also be unstable in the inner magnetosphere, associated with localized flow channels (Chaston, 2022).

In the case of unmagnetized planets such as Mars and Venus, that do not have a global intrinsic magnetic field, the velocity-sheared boundary appears between the shocked solar wind and the ionized upper atmosphere (ionosphere), i.e., around the ionopause. The magnetic field geometry effects are also important at Venus and Mars, and KHI is mainly excited in the perpendicular plane to the IMF (Dang et al., 2022). Due to the large density in the ionosphere, the compressibility effects are expected to be important and can suppress the occurrence of KHI. Despite this expectation from theory, KHI vortex-like signatures (boundary waves) have been observed on Mars (Ruhunusiri et al., 2016; Poh et al., 2021; Wang et al., 2022) and Venus (Chong et al., 2018), where r_n is larger than in the terrestrial case.

Particularly on Mars, r_n tends to be large due to the low solar wind density, compared to Venus, at the Martian orbit ($r_n >$ 1000), and KHI is expected to be stabilized by compressibility (Miura and Pritchett, 1982). Thus, the observation of KHI-like signatures around the Martian ionopause poses a fundamental question about the ubiquity of KHI in space plasmas, where a large density gradient across velocity-sheared boundaries is sometimes expected: What enables the KHI excitation even at a plasma boundary with a large density gradient? Understanding of the characteristics of KHI around the ionopause is also important for comprehending the ionospheric cold ion outflows from the Martian atmosphere (Inui et al., 2019)

Using a comprehensive *in situ* plasma observation at Mars by MAVEN and MHD simulations of KHI, in this study, we investigate the characteristics of plasma boundaries with large density gradients and their effects on Kelvin–Helmholtz instability. Following the description of the instrumentation and model in Section 2, the results of the comparison between the observations and simulations are shown in Section 3. Based on observations, we propose a new realistic boundary structure for the velocity-sheared layer with a large density gradient based on entropy and conduct MHD simulations of KHI. In Section 4 and Section 5, discussions and conclusion are provided, respectively.

2 Instrumentation and model description

A comprehensive *in situ* observation of plasma at Mars by MAVEN (Andersson et al., 2015; Connerney et al., 2015; Halekas et al., 2015; McFadden et al., 2015) provides an ideal opportunity to investigate the fundamental question described in Section 1. We used the data obtained in the MAVEN orbit #118 on 20 October 2014 from the MAG instrument (Connerney et al., 2015) for the vector magnetic fields, STATIC (McFadden et al., 2015)/SWIA (Halekas et al., 2015) for ion moments with/without mass discrimination, and LPW (Andersson et al., 2015) for electron density in the ionosphere. We used SWIA density and velocity data only for the time period when the SupraThermal and Thermal Ion Composition (STATIC) energy coverage was limited due to its observation mode, as described in Section 3.1.

A high-resolution, numerically robust magnetohydrodynamic (MHD) simulation code CANS+ (Matsumoto et al., 2019) is used to simulate KHI in velocity-sheared boundary layers with large density gradients. The nonlinear evolution of the physical quantities—plasma number density, pressure, velocity, and magnetic field B—is followed on the basis of MHD equations. We numerically solve the equations by using the fifth-order MP5 scheme (Suresh and Huynh, 1997) and the approximate Rieman solver of the HLLD scheme (Miyoshi and Kusano, 2005). In order to compare traditional density-based and new entropy-based initial structures of the velocity-sheared boundary, we conducted two sets of two-dimensional MHD simulations. Two models of the boundary structure will be described in detail, together with observations, in Section 3.1. Based on the observations, the number density, velocity, temperature, and magnetic field strength in the shocked solar wind (ionosphere) side are set to 2 (10^4) cm^{-3}, 177 (0) km/s, 275 (0.055) eV, and 8 (8) nT, respectively. It corresponds to r_n = 5000. The total number of grid points used is 504 × 600. The spatial resolution

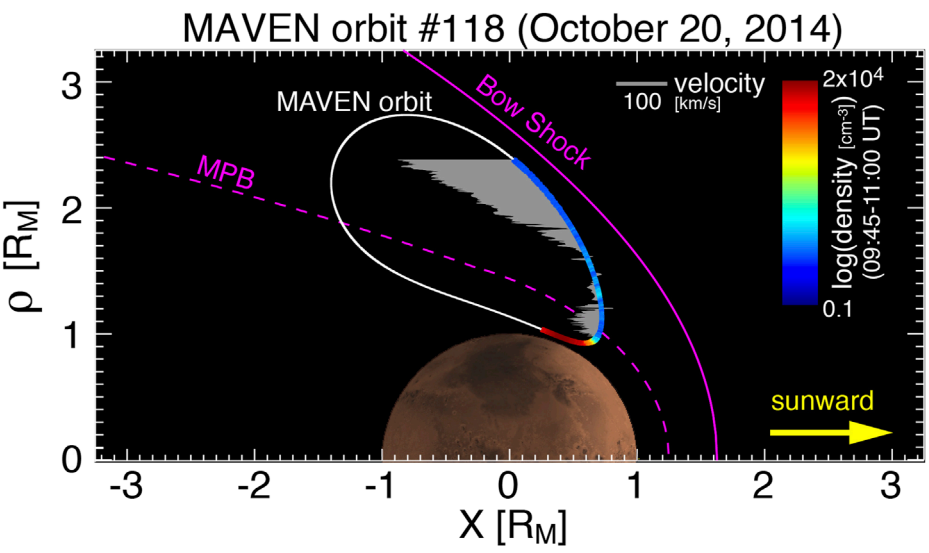

FIGURE 1
Orbital configuration of the MAVEN spacecraft around Mars during 07:30–12:07 UT on 20 October 2014 (orbit #118). The x-axis points sunward from the center of Mars, and ρ indicates the distance from the X axis in units of the Martian radius, R_M. Solid and dashed magenta lines display typical bow shock and magnetic pile-up boundary (MPB) (Trotignon et al., 2006) locations, respectively. The white line shows the MAVEN orbital projection onto the X -ρ coordinates. For the period from 09:45 to 11:00 UT, which corresponds to the time period shown in Figure 2, the total ion density is color-coded on the orbit. Horizontal gray thin lines show the center of the mass ion velocity component parallel to the perpendicular flow in the shocked solar wind.

is set as $\Delta x = \Delta y = 1/24$. Thus, the velocity shear layer is resolved with about 48 grids, and the resolution is good enough to reproduce the linear growth of KHI (Matsumoto et al., 2019). The settings for the two simulation runs other than the initial conditions are identical.

3 Results

3.1 Boundary observations by MAVEN and the entropy-based boundary structure model

Since Mars does not possess a global magnetic field, the solar wind directly interacts with the ionosphere. As it approaches Mars, the supersonic solar wind forms a bow shock in front of the planet (Figure 1), and the decelerated, shocked solar wind interacts with the dense ionosphere. At the boundary between the shocked solar wind and the ionosphere, the density gradient is large, with a typical density ratio of $r_n \sim 1000$. A combination of mechanical and electrostatic attenuators of the STATIC instrument onboard MAVEN (McFadden et al., 2015) enables continuous ion density measurements over four orders of magnitude, which is essential in order to reveal the detailed structure inside the boundary.

MAVEN observed an example of a velocity-sheared boundary with a large density gradient of $r_n \sim 5000$ between the shocked solar wind and dayside Martian ionosphere, as shown by the color codes and gray bars in Figure 1. The magnetic field in the ionosphere (light blue bar at the bottom in Figure 2) and shocked solar wind (orange) has a similar value (−8 nT) with some enhancement inside the boundary (the top panel in Figure 2). The high magnetic field strength at low altitudes is due to the localized crustal magnetic fields and will not have major effects on the global boundary structure. Alternating high and low energy populations are seen inside the boundary (second and third panels from the top of Figure 2), and increases in heavy ions at masses of −16 (O^+) and 32 (O_2^+) coincide with the low energy populations (not shown). It is consistent with the density variations of each ion species shown in the fifth panel in Figure 2, i.e., O_2^+ is dominant in the ionosphere, while proton contribution is important in the shocked solar wind side. As the spacecraft traverses from the ionosphere to the shocked solar wind, the velocity increases from −0 to −177 km/s (sixth panel in Figure 2), while the density decreases from −6570 to 1.3 cm^{-3} (5th panel), i.e., $r_n \sim 5000$, by taking averages for each region.

In order to investigate the location of the velocity shear relative to the density gradient, the observed relation between the density and velocity is determined and plotted in Figure 3A. In theoretical considerations (Miura and Pritchett, 1982; Amerstorfer et al., 2010; Matsumoto and Seki, 2010), the velocity shear, taking the X-axis in the original shocked solar wind direction and Y across the shear, is often expressed with the hyperbolic tangent as

$$V_x = -(V_0/2)\{1 + \tanh(y/L)\},$$

in the rest frame of the ionosphere, where V_0 and L indicate velocity in the shocked solar wind and the half-width of the shear layer, respectively. In the case of a density gradient, previous studies (Amerstorfer et al., 2010; Matsumoto

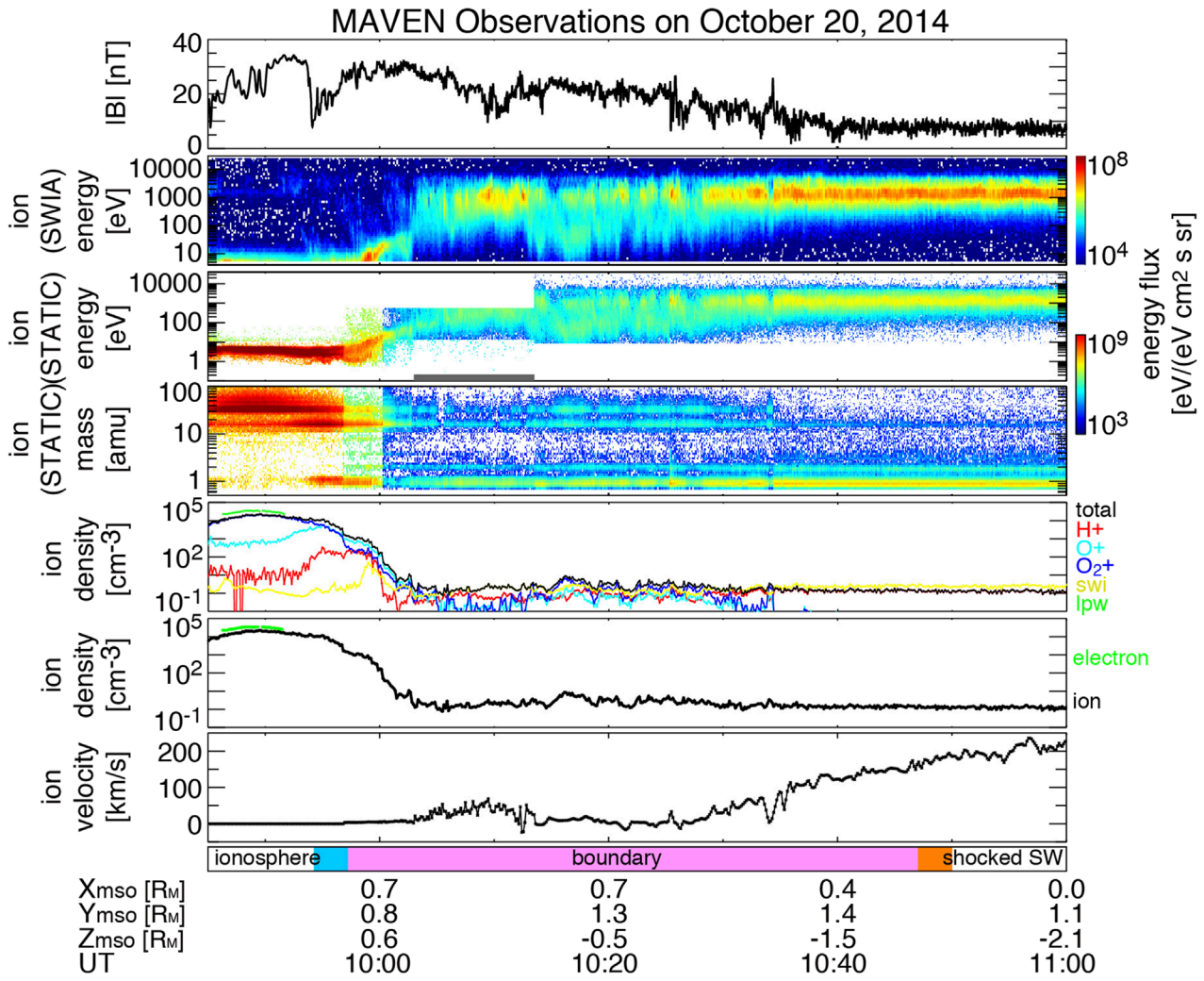

FIGURE 2
Summary of MAVEN observations in a large density gradient boundary between the shocked solar wind and the ionosphere. From the top of the figure, each panel shows magnetic field strength from the MAG instrument (Connerney et al., 2015), the ion energy–time, mass–time spectrograms, density of each species, combined electron/ion density, velocity, and region identification bar, respectively. The black line in the sixth panel of the ion density shows the total ion density obtained both from STATIC (McFadden et al., 2015) and SWIA (Halekas et al., 2015) in addition to electron density from LPW (Andersson et al., 2015) in the ionosphere (green) to confirm the accuracy of the density observation. The ion velocity panel displays the bulk velocity component in the direction of the shocked solar wind flow averaged over the orange bar time interval at the bottom. Note that we used SWIA density and velocity data for the time period shown in the gray bar at the bottom of the third panel due to the limited energy coverage of STATIC. The bottom color bar indicates time intervals used in the data analysis. Light blue (orange) corresponds to the interval used to calculate ionospheric (shocked solar wind) parameters, while pink indicates the boundary region in which the velocity shear and density gradient are observed.

and Seki, 2010) have assumed that the density gradient is expressed as

$$n = (n_{io}/2)\{1 - \tanh(y/L)\} + (n_{sw}/2)\{1 + \tanh(y/L)\},$$

where n_{io} and n_{sw} show number densities in the ionospheric and shocked solar wind sides, respectively. This traditional density-based model of the velocity-sheared boundary is displayed in Figure 4A and also by the blue line in Figure 3A. The observation therefore reveals that the observed density–velocity relation (black dots in Figure 4A) at the boundary with a large density gradient differs largely from the density-based model (blue line).

In order to describe the observed boundary structure, we here introduce the entropy per unit mass, S ($= P/n^{5/3}$, where P indicates the thermal pressure), instead of the density, to construct an entropy-based model:

$$S = (S_{io}/2)\{1 - \tanh(y/L)\} + (S_{sw}/2)\{1 + \tanh(y/L)\}, \text{and } n = (P/S)^{3/5},$$

where S_{io} and S_{sw} show the entropy in the ionospheric and shocked solar wind sides, respectively. Figure 3A shows that the density–velocity relation with this entropy-based model (red line)

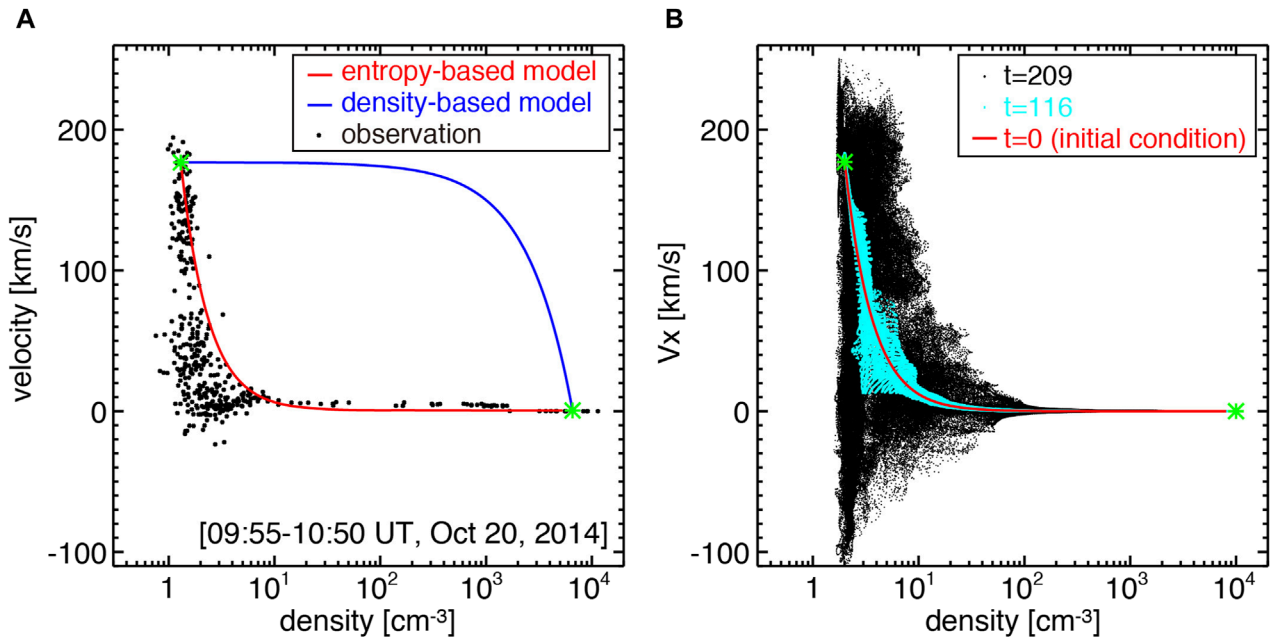

FIGURE 3
Relations between ion density and velocity **(A)** observed in the large-density gradient boundary by MAVEN and **(B)** obtained in the MHD simulation with the entropy-based model as the initial condition. In panel **(A)**, black dots show the ion density and velocity in the boundary interval observed by MAVEN (the same data shown in Figure 2 for the time interval indicated by the pink bar at the bottom of Figure 2), while red and blue lines display the newly proposed entropy-based model and classical density-based model, respectively, calculated based on parameters (green symbols) derived from observations in both ends of the boundary, i.e., the shocked solar wind (high speed and low density) and the ionosphere (low speed and high density). In panel **(B)**, light blue and black dots indicate different time evolution stages, i.e., $t =$ 116 (linear stage of the KHI development) and 209 (nonlinear stage), respectively, of the simulation run with the initial condition obtained from the observation-based entropy-based model (red line). We assumed L = 50 km for the calculation of t.

agrees much better with observations than the density-based model (blue). It should be noted that the entropy is calculated under the assumption that the pressure is constant across the boundary. We investigated other MAVEN orbits that had comprehensive plasma data, including low-energy range observations by STATIC around the periapsis, which were available between 1 December 2014 and 26 January 2015. The observations show that all of the investigated boundary structure observations agree better with the entropy-based model than the density-based model. Compared to other physical parameters, such as momentum, to construct a new model, the entropy-based model shows the best agreement with the observation. We think it is natural to consider the boundary structure in which the entropy varies with the velocity since the density perturbation is theoretically transported by the entropy mode wave in the MHD approximation. In the next section, we use the traditional density-based and new entropy-based models as the initial conditions of the KHI simulations to observe the effects of the boundary model on momentum and mass transfers across the boundary by KHI.

3.2 MHD simulation results

We here conducted two-dimensional MHD simulations of KHI with a transverse magnetic field for the two initial conditions, i.e., the density-based model (Figure 4A) and entropy-based model (Figure 4B). The density, velocity, temperature, and magnetic field strength in the shocked solar wind (ionosphere) side are set to 2 (10^4) cm^{-3}, 177 (0) km/s, 275 (0.055) eV, and 8 (8) nT based on observations shown in Section 3.1, respectively. These parameters correspond to $r_n = 5000$. The settings for the two simulation runs other than the initial conditions are identical. Figure 3B shows the time evolution with the entropy-based initial condition (red line) at the early (light blue dots) and fully developed (black dots) stages of the KHI time evolution. The observed density–velocity relation (black dots in Figure 3A) resembles that of the early-stage KHI (light blue in Figure 3B), suggesting that KHI had already started to grow in the real Martian boundary.

The center upper part of Figure 4D shows a well-developed vortex with its center at approximately $(X, Y) = (14, 2)$. The velocity of the vortex along the boundary was approximately 62 km/s. In contrast to the KHI vortex development with the entropy-based model in Figure 4D, we did not see any clear growth of KHI in the case of the density-based model (Figure 4C). In the density-based boundary structure, the magnetosonic Mach number M_f (defined by the speed of sound c_s and Alfvén velocity v_A as $M_f = V_0/\sqrt{{c_s}^2 + {v_A}^2}$), in most parts of the velocity shear, becomes large enough ($M_f > 2$) to suppress the KHI growth due to the compressibility (Miura and Pritchett, 1982). A remarkable difference between the density-based

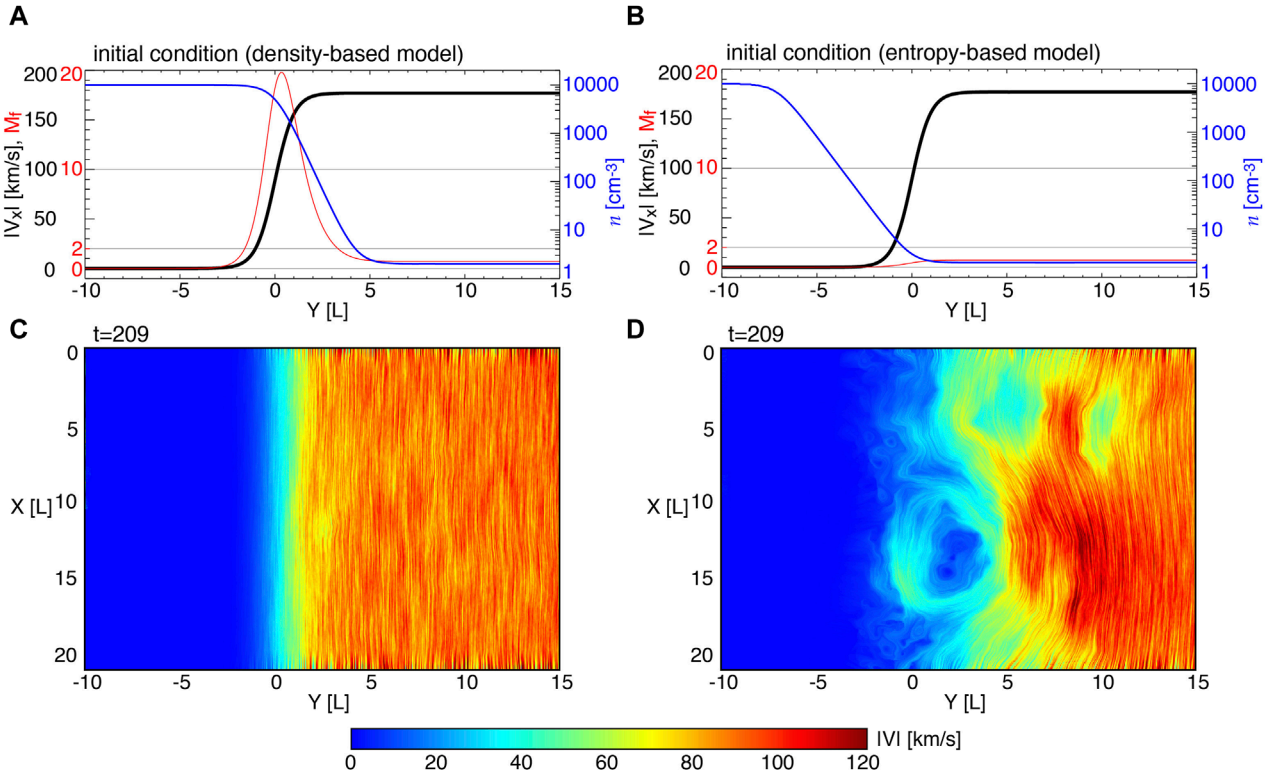

FIGURE 4
Comparison between MHD simulations with two different boundary structures (red and blue lines in Figure 3A) as initial conditions. Panels **(A)** and **(C)** and **(B)** and **(D)** correspond to the density-based model and entropy-based model cases, respectively. Top panels show initial profiles of velocity (black line), density (blue), and the magnetosonic Mach number M_f (red) across the boundary in Y normalized with the initial width of the velocity shear layer: L. In these two cases, the velocity shear profile and physical values on each side of the shear layer are the same. On one hand, the relative location of the velocity shear to the large density gradient is different in the two cases, and the stability condition for KHI ($M_f > 2$) is satisfied in most of the velocity shear region in the density-based model **(A)**, as described in the text. Bottom panels display the flow pattern using the line integral convolution (LIC) technique (Cabral and Leedom, 1993) in the simulation domain at $t =$ 209, where a KHI vortex is developed in panel **(D)**, but not in panel **(C)**. The |V| profile with white noise was used as a texture for LIC visualization.

and entropy-based models is the relative location of the velocity shear to the density gradient. As shown in Figure 4, the entropy-based model places the velocity shear in the lower-density region, i.e., the speed of sound at the center of the velocity shear can be larger, i.e., M_f is smaller than in the density-based model. It thus weakens the compressibility suppression effect and enables KHI excitation.

4 Discussion

The real boundary structure with velocity shear and density gradient in space plasma reported here requires alteration of the initial boundary structure in theoretical studies of KHI to estimate mass and momentum transport across the boundary. In collisionless space plasmas, plasma mixing across the magnetic field lines occurs at small-scale structures, caused by secondary instabilities excited in the rolled-up vortex of KHI, i.e., at a well-developed KHI. To understand the momentum and mass transport mechanisms across the velocity-sheared boundary, high-resolution kinetic simulations of KHI have been conducted (Matsumoto and Seki, 2010; Dargent et al., 2019). Some of the previous studies have identified the importance of including electron inertial effects when assessing mass transport mechanisms across the boundaries. The observed entropy-based boundary structure presented here has a fundamental difference from the traditional initial conditions of the various simulation studies of KHI (density-based model) (Suresh and Huynh, 1997; Casanova et al., 2011; Andersson et al., 2015; Matsumoto et al., 2019; Hwang et al., 2023). The change in the initial condition largely alters the time evolution of KHI, even in the small and moderate density gradient cases. For example, the usage of the proposed entropy-based model based on the observations will be important for understanding the interplay between KHI and the lower-hybrid drift instability in plasma mixing (Dargent et al., 2019).

Although kinetic particle-in-cell (PIC) simulations are important to investigate plasma mixing processes, MHD (Michael et al., 2021; Dang et al., 2022) or hybrid (Wang et al., 2023) simulations have the advantage of conducting three-dimensional global simulations of the interaction between the solar wind and

planetary magnetosphere/ionosphere. The comparison between MHD and PIC simulations indicates that the MHD approximation can capture important features of the plasma mixing layer in certain conditions when the grid resolution and numerical dissipation are small enough (Matsumoto and Seki, 2010). Thus, this study encourages investigations of dayside velocity-sheared boundary structures in the global simulation, which determine the initial condition for KHI growth, to compare them with the entropy-based boundary structure obtained from observations in this study.

The specific entropy S used to formulate the realistic boundary structure proposed in this study has been utilized to explore transport of plasma from the solar wind to various regions in the Earth's magnetosphere (Borovsky and Cayton, 2011). S is a conserved quantity in the adiabatic transport of isotropic plasma, and it is often used to track plasma transport, i.e., there is often a gap of S across the boundaries. Non-conservation of S is expected when nonadiabatic processes such as plasma mixing and wave–particle interaction occur. In the MHD approximation, the density perturbation is transported by the entropy mode. We thus think that it is a reasonable choice for the velocity-sheared boundary model to assume that S varies with velocity in the boundary.

The entropy-based model obtained in this study has no artificial peak in the magnetosonic Mach number M_f and momentum inside the boundary, in contrast to the density-based model, as shown by the red lines in Figures 4A,B. It prevents the overestimation of mass and momentum transport. The observation also indicates that the realistic boundary structure in space plasma can facilitate KHI over a wide range of density gradients by evading compressibility suppression, and thus enabling the ubiquitous occurrence of Kelvin–Helmholtz instability in the plasma universe. It might explain the KHI occurrence reported in various space and astrophysical plasmas (Hasegawa et al., 2004; Price and Rosswog, 2006; Slavin et al., 2008; Berne et al., 2010; Casanova et al., 2011; Delamere et al., 2013; Hillier and Arregui, 2019). Specific to Mars, KHI excitation can cause cold ions to escape from the Martian ionosphere (Inui et al., 2019), and it might provide a new escape channel to answer the mystery of the fate of its ancient carbon dioxide (Barabash et al., 2007) and understand the ancient Martian climate change (Jakosky et al., 2018).

5 Conclusion

Based on comprehensive plasma observations by MAVEN at Mars, we investigated the real structure of velocity-sheared boundaries with a large density gradient (density ratio of 5000), and the two cases of MHD simulations of KHI with two different initial boundary structure models are compared. The results are as follows:

- The observations show that the boundary structure has a fundamental difference from the traditional density-based model used in previous simulation studies. Based on the observations, a new entropy-based boundary model is proposed.
- In the proposed entropy-based model, the relative location of the velocity shear to the density gradient changed so that the velocity shear is located in the lower-density region than in the density-based model.
- The comparison between simulations with two boundary models shows that KHI cannot develop in the density-based boundary model, while it can be excited in the entropy-based model due to the difference in compressibility effects at the velocity shear layer.

These results suggest that the suppression of KHI can be weakened in the realistic velocity-sheared boundary structure even when the density gradient across the boundary is large, and it can facilitate the ubiquitous occurrence of Kelvin–Helmholtz instability in various planetary magnetospheres and astrophysical plasmas. It will be useful to use the entropy-based boundary model for future simulation studies of velocity-sheared boundaries with a density gradient.

Data availability statement

The datasets presented in this study can be found in online repositories. The names of the repository/repositories and accession number(s) can be found below. The Mars Atmosphere and Volatile EvolutioN (MAVEN) data are available from the NASA Planetary Data System (https://pds.nasa.gov) and the MAVEN Science Data Center (https://lasp.colorado.edu/maven/sdc/public/). The simulation data used in this study are available from the UTokyo Repository (https://repository.dl.itc.u-tokyo.ac.jp/).

Author contributions

KS: conceptualization, formal analysis, funding acquisition, investigation, methodology, project administration, visualization, writing–original draft, and writing–review and editing. YM: investigation, methodology, validation, visualization, writing–review and editing, writing–original draft, and software. NT: conceptualization, validation, and writing–review and editing. TH: formal analysis, validation, writing–review and editing, and software. DB: validation, writing–review and editing, and investigation. HN: funding acquisition, writing–review and editing, and validation. JM: data curation, software, supervision, validation, and writing–review and editing. JH: data curation, validation, and writing–review and editing. SR: investigation and writing–review and editing. DM: data curation and writing–review and editing. LA: data curation, validation, writing–review and editing, and investigation. JE: data curation, validation, and writing–review and editing. DB: supervision and writing–review and editing. JL: supervision, writing–review and editing, and investigation. BJ: funding acquisition, resources, supervision, writing–review and editing, and project administration.

Funding

The author(s) declare that financial support was received for the research, authorship, and/or publication of this article. This work is conducted under NASA's MAVEN Participating Scientist Program (Proposal #12-MAVENPS12-0017, PI: KS). This work was supported by a Grant-in-Aid for Scientific Research (A) #20H00192 and #22H00164 and Fostering Joint International Research (B) 18KK0093 by the Japan Society for the Promotion of Science.

Acknowledgments

The authors thank M. Fujimoto for useful discussion and J. E. P. Connerney for his contribution to MAG data.

Conflict of interest

The authors declare that the research was conducted in the absence of any commercial or financial relationships that could be construed as a potential conflict of interest.

Publisher's note

All claims expressed in this article are solely those of the authors and do not necessarily represent those of their affiliated organizations, or those of the publisher, the editors, and the reviewers. Any product that may be evaluated in this article, or claim that may be made by its manufacturer, is not guaranteed or endorsed by the publisher.

References

Amerstorfer, U. V., Erkaev, N. V., Taubenschuss, U., and Biernat, H. K. (2010). Influence of a density increase on the evolution of the Kelvin–Helmholtz instability and vortices. *Phys. Plasmas* 17, 072901. doi:10.1063/1.3453705

Andersson, L., Ergun, R. E., Delory, G. T., Eriksson, A., Westfall, J., Reed, H., et al. (2015). The Langmuir probe and waves (LPW) instrument for MAVEN. *Space Sci. Rev.* 195, 173–198. doi:10.1007/s11214-015-0194-3

Barabash, S., Fedorov, A., Lundin, R., and Sauvaud, J. A. (2007). Martian atmospheric erosion rates. *Science* 315, 501–503. doi:10.1126/science.1134358

Berne, O., Marcelino, N., and Cernicharo, J. (2010). Waves on the surface of the Orion molecular cloud. *Nature* 466, 947–949. doi:10.1038/nature09289

Borovsky, J. E., and Cayton, T. E. (2011). Entropy mapping of the outer electron radiation belt between the magnetotail and geosynchronous orbit. *J. Geophys. Res.* 116, A06216. doi:10.1029/2011JA016470

Cabral, B., and Leedom, L. C. (1993). "Imaging vector fields using line integral convolution," in Proceedings of the 20th annual conference on Computer graphics and interactive techniques (SIGGRAPH 93), 263–270.

Casanova, J., José, J., García-Berro, E., Shore, S. N., and Calder, A. C. (2011). Kelvin–Helmholtz instabilities as the source of inhomogeneous mixing in nova explosions. *Nature* 478, 490–492. doi:10.1038/nature10520

Chaston, C. C. (2022). Flow channels and the generation of Alfvenic turbulence along storm-time inner magnetospheric field-lines. *Geophys. Res. Lett.* 49, e2022GL101321. doi:10.1029/2022GL101321

Chong, G. S., Pope, S., Walker, S. N., Frahm, R. A., Zhang, T. L., and Futaana, Y. (2018). A statistical study of ionospheric boundary wave formation at Venus. *J. Geophys. Res.* 123, 7668–7685. doi:10.1029/2018JA025644

Connerney, J. E. P., Espley, J., Lawton, P., Murphy, S., Odom, J., Oliversen, R., et al. (2015). The MAVEN magnetic field investigation. *Space Sci. Rev.* 195, 257–291. doi:10.1007/s11214-015-0169-4

Dang, T., Lei, J., Zhang, B., Zhang, T., Yao, Z., Lyon, J., et al. (2022). Oxygen ion escape at Venus associated with three-dimensional Kelvin-Helmholtz instability, *Geophys. Res. Lett.* 49, e2021GL096961. doi:10.1029/2021GL096961

Dargent, J., Lavorenti, F., Califano, F., Henri, P., Pucci, F., and Cerri, S. S. (2019). Interplay between Kelvin Helmholtz and lower-hybrid drift instabilities. *J. Plasma Phys.* 85, 805850601. doi:10.1017/S0022377819000758

Delamere, P. A., Wilson, R. J., Eriksson, S., and Bagenal, F. (2013). Magnetic signatures of Kelvin-Helmholtz vortices on Saturn's magnetopause: global survey. *J. Geophys. Res.* 118, 393–404. doi:10.1029/2012JA018197

Fujimoto, M., and Terasawa, T. (1994). Anomalous ion mixing within an MHD scale Kelvin-Helmholtz vortex. *J. Geophys. Res.* 99, 8601–8613. doi:10.1029/93ja02722

Halekas, J. S., Taylor, E. R., Dalton, G., Johnson, G., Curtis, D. W., McFadden, J. P., et al. (2015). The solar wind ion analyzer for MAVEN. *Space Sci. Rev.* 195, 125–151. doi:10.1007/s11214-013-0029-z

Hasegawa, H., Fujimoto, M., Phan, T. D., Rème, H., Balogh, A., Dunlop, M. W., et al. (2004). Transport of solar wind into Earth's magnetosphere through rolled-up Kelvin–Helmholtz vortices. *Nature* 430, 755–758. doi:10.1038/nature02799

Hillier, A., and Arregui, I. (2019). Coronal cooling as a result of mixing by the nonlinear kelvin–helmholtz instability. *ApJ* 885, 101. doi:10.3847/1538-4357/ab4795

Hwang, K.-J., Wang, C.-P., Nykyri, K., Hasegawa, H., Tapley, M. B., Burch, J. L., et al. (2023). Kelvin-Helmholtz instability-driven magnetopause dynamics as turbulent pathway for the solar wind-magnetosphere coupling and the flank-central plasma sheet communication. *Front. Astron. Space Sci.* 10, 1151869. doi:10.3389/fspas.2023.1151869

Inui, S., Seki, K., Sakai, S., Brain, D. A., Hara, T., McFadden, J. P., et al. (2019). Statistical study of heavy ion outflows from Mars observed in the Martian-induced magnetotail by MAVEN. *J. Geophys. Res.* 124, 5482–5497. doi:10.1029/2018JA026452

Jakosky, B. M., Brain, D., Chaffin, M., Curry, S., Deighan, J., Grebowsky, J., et al. (2018). Loss of the Martian atmosphere to space: present-day loss rates determined from MAVEN observations and integrated loss through time. *Icarus* 315, 146–157. doi:10.1016/j.icarus.2018.05.030

Kavosi, S., Raeder, J., Johnson, J. R., Nykyri, K., and Farrugia, C. J. (2023). Seasonal and diurnal variations of Kelvin-Helmholtz Instability at terrestrial magnetopause. *Nat. Comm.* 14, 2513. doi:10.1038/s41467-023-37485-x

Matsumoto, Y., Asahina, Y., Kudoh, Y., Kawashima, T., Matsumoto, J., Takahashi, H. R., et al. (2019). Magnetohydrodynamic simulation code CANS+: assessments and applications. *Publ. Astron. Soc. Jpn.* 71. doi:10.1093/pasj/psz064

Matsumoto, Y., and Seki, K. (2010). Formation of a broad plasma turbulent layer by forward and inverse energy cascades of the Kelvin-Helmholtz instability. *J. Geophys. Res.* 115, A10231. doi:10.1029/2009JA014637

Matthaeus, W. H., Qin, G., Bieber, J. W., and Zank, G. P. (2003). Nonlinear collisionless perpendicular diffusion of charged particles. *Astrophys. J.* 590, L53–L56. doi:10.1086/376613

McFadden, J. P., Kortmann, O., Curtis, D., Dalton, G., Johnson, G., Abiad, R., et al. (2015). MAVEN SupraThermal and thermal ion compostion (STATIC) instrument. *Space Sci. Rev.* 195, 199–256. doi:10.1007/s11214-015-0175-6

Michael, A. T., Sorathia, K. A., Merkin, V. G., Nykyri, K., Burkholder, B., Ma, X., et al. (2021). Modeling Kelvin-Helmholtz instability at the high latitude boundary layer in a global magnetosphere simulation. *Geophys. Res. Lett.* 48, e2021GL094002. doi:10.1029/2021GL094002

Miura, A., and Pritchett, P. L. (1982). Nonlocal stability analysis of the MHD Kelvin-Helmholtz instability in a compressible plasma. *J. Geophys. Res.* 87, 7431–7444. doi:10.1029/ja087ia09p07431

Miyoshi, T., and Kusano, K. (2005). A multi-state HLL approximate Riemann solver for ideal magnetohydrodynamics. *J. Comput. Phys.* 208, 315–344. doi:10.1016/j.jcp.2005.02.017

Poh, G., Espley, J. R., Nykyri, K., Fowler, C. M., Ma, X., Xu, S., et al. (2021). On the growth and development of nonlinear Kelvin–Helmholtz instability at Mars: MAVEN observations. *J. Geophys. Res.* 126, e2021JA029224. doi:10.1029/2021JA029224

Price, D. J., and Rosswog, S. (2006). Producing ultrastrong magnetic fields in neutron star mergers. *Science* 312, 719–722. doi:10.1126/science.1125201

Ruhunusiri, S., Halekas, J. S., McFadden, J. P., Connerney, J. E. P., Espley, J. R., Harada, Y., et al. (2016). MAVEN observations of partially developed Kelvin-Helmholtz vortices at Mars. *Geophys. Res. Lett.* 43, 4763–4773. doi:10.1002/2016gl068926

Seki, K., Hirahara, M., Hoshino, M., Terasawa, T., Elphic, R. C., Saito, Y., et al. (2003). Cold ions in the hot plasma sheet of Earth's magnetotail. *Nature* 422, 589–592. doi:10.1038/nature01502

Slavin, J. A., Acuna, M. H., Anderson, B. J., Baker, D. N., Benna, M., Gloeckler, G., et al. (2008). Mercury's magnetosphere after MESSENGER's first flyby. *Science* 321, 85–89. doi:10.1126/science.1159040

Suresh, A., and Huynh, H. T. (1997). Accurate monotonicity-preserving schemes with Runge–Kutta time stepping. *J. Comput. Phys.* 136, 83–99. doi:10.1006/jcph.1997.5745

Trotignon, J. G., Mazelle, C., Bertucci, C., and Acuña, M. (2006). Martian shock and magnetic pile-up boundary positions and shapes determined from the Phobos 2 and Mars Global Surveyor data sets. *Planet. spa. Sci.* 52, 357–369. doi:10.1016/j.pss.2006.01.003

Wan, W. C., Malamud, G., Shimony, A., Di Stefano, C., Trantham, M., Klein, S., et al. (2015). Observation of single-mode, kelvin-helmholtz instability in a supersonic flow. *Phys. Rev. Lett.* 115, 145001. doi:10.1103/PhysRevLett.115.145001

Wang, L., Huang, C., Du, A., Ge, Y., Chen, G., Yang, Z., et al. (2023). Kelvin–helmholtz instability at Mars: *in situ* observations and kinetic simulations. *Astrophys. J.* 947, 51. doi:10.3847/1538-4357/acc655

Wang, X., Xu, X., Ye, Y., Wang, J., Wang, M., Zhou, Z., et al. (2022). MAVEN observations of the Kelvin-Helmholtz instability developing at the ionopause of Mars. *Geophys. Res. Lett.* 49, e2022GL098673. doi:10.1029/2022GL098673